Draft version May 7, 2016
Preprint typeset using LaTeX style emulateapj v. 08/22/09

arXiv:0712.1038v1 [astro-ph] 6 Dec 2007

EXTENDED ANOMALOUS FOREGROUND EMISSION IN THE WMAP 3-YEAR DATA

Gregory Dobler[1,2] & Douglas P. Finkbeiner[1]

Draft version May 7, 2016

ABSTRACT

We study the spectral and morphological characteristics of the diffuse Galactic emission in the WMAP temperature data using a template-based multi-linear regression, and obtain the following results. 1. We confirm previous observations of a bump in the dust-correlated spectrum, consistent with the Draine & Lazarian spinning dust model. 2. We also confirm the "haze" signal in the inner Galaxy, and argue that it does not follow a free–free spectrum as first thought, but instead is synchrotron emission from a hard electron cosmic-ray population. 3. In a departure from previous work, we allow the spectrum of Hα-correlated emission (which is used to trace the free–free component) to float in the fit, and find that it does not follow the expected free–free spectrum. Instead there is a bump near 50 GHz, modifying the spectrum at the 20% level, which we speculate is caused by spinning dust in the warm ionized medium. 4. The derived cross-correlation spectra are not sensitive to the map zero points, but are sensitive to the choice of CMB estimator. In cases where the CMB estimator is derived by minimizing variance of a linear combination of the WMAP bands, we show that a bias proportional to the cross-correlation of each template and the true CMB is always present. This bias can be larger than any of the foreground signals in some bands. 5. Lastly, we consider the frequency coverage and sensitivity of the *Planck* mission, and suggest linear combination coefficients for the CMB template that will reduce both the statistical and systematic uncertainty in the synchrotron and haze spectra by more than an order of magnitude.

Subject headings: diffuse radiation — dust, extinction — ISM: clouds — radiation mechanisms: non-thermal — radio continuum: ISM

1. INTRODUCTION

Observations of the cosmic microwave background (CMB) by the *Wilkinson Microwave Anisotropy Probe* (WMAP) have revolutionized our understanding of cosmology and placed strong constraints on cosmological parameters (Spergel et al. 2003, 2007; Tegmark et al. 2004). Moreover, the WMAP foreground signal represents the most detailed and sensitive full-sky maps of Galactic microwave emission, providing an enormous wealth of information about the physical processes in the interstellar medium (ISM).

1.1. *Galactic emission mechanisms*

There are three well established types of Galactic foreground signals at WMAP frequencies: free–free (or thermal bremsstrahlung) emission from interaction of free electrons with ions, dust emission from grains heated by the surrounding radiation field, and synchrotron emission from supernova shock accelerated electrons. In addition, there are two other emission mechanisms which have proven more difficult to characterize: spinning dust and the anomalous "haze" (Finkbeiner 2004). Spinning dust refers to emission from the smallest dust grains which have non-negligible electric dipole moments and are excited into rotational modes through a variety of mechanisms (cf. Draine & Lazarian 1998b). The physical origin of the haze is uncertain.

Though initially controversial (Bennett et al. 2003), numerous authors have presented evidence for a spinning dust spectrum when combining WMAP data with external data sets (de Oliveira-Costa et al. 2004; Finkbeiner, Langston, & Minter 2004; Boughn & Pober 2007). Using only WMAP data, Bennett et al. (2003) and Hinshaw et al. (2007) point out that it is difficult to spectrally distinguish certain spinning dust models from synchrotron. However, in our companion paper (Dobler & Finkbeiner 2007, hereafter DF07), we show that a spinning dust spectrum is indeed recoverable using exclusively WMAP data, though it is not spatially correlated with the *thermal* dust emission.

The haze was originally thought (Finkbeiner 2004) to be free–free emission from ionized gas which is too hot to be visible in recombination line maps and too cold to be visible in X-ray maps. However, gas at the required temperature $T \sim 10^5$ K is thermally unstable (Spitzer 1978). Furthermore, we will show in §3 that the spectrum of the haze is inconsistent with free–free emission and is most likely explained as a hard synchrotron component which is morphologically and spectrally distinct from the above mentioned *soft* synchrotron.

1.2. *MEM analysis*

With the first and third year data releases, the WMAP team provided a dual foreground analysis: a maximum entropy method (MEM) and a template fitting algorithm. The former was intended to improve our understanding of the astrophysics of foreground emission while the latter (more statistically stable) algorithm was meant to produce CMB maps with well characterized noise properties for use in the cosmological analysis (Bennett et al. 2003; Hinshaw et al. 2007).

Although the total observed emission matches the MEM model to better than 1%, "Low residual solu-

[1] Institute for Theory and Computation, Harvard-Smithsonian Center for Astrophysics, 60 Garden Street, MS-51, Cambridge, MA 02138 USA
[2] gdobler@cfa.harvard.edu

tions are highly constrained, but not necessarily unique or correct" (Bennett et al. 2003, p. 108). The MEM method is a pixel-by-pixel fit which minimizes the functional $H(p) = A(p) + \lambda(p)B(p)$ (Press et al. 1992) where λ is a regularizing parameter,

$$A(p) = \chi^2(p) = \sum_p [T(\nu, p) - T_m(\nu, p)]^2/\sigma^2, \quad (1)$$

$$B(p) = \sum_c T_c(p) \ln[T_c(p)/P_c(p)], \quad (2)$$

and the sum is over Galactic emission components. $P_c(p)$ is a prior template for component c, normalized to the same frequency as T_c (see Bennett et al. 2003; Hinshaw et al. 2007, for details).

The noise properties of a MEM-derived CMB map are complicated, e.g. by the fact that noise is clipped to be non-negative by the logarithm in Equation 2. Because simple noise properties are desirable for a cosmological power spectrum analysis, a template-based map is used instead. In the end, Bennett et al. (2003) and Hinshaw et al. (2007) fit spatial templates for the dust, free–free, and synchrotron ISM emissions to WMAP Q, V, and W bands. They find that the remaining contamination in the maps is sufficiently subdominant outside the Kp2 mask so that the effect on the CMB power spectrum is negligible.

1.3. *"Anomalous" ISM emission mechanisms*

Given their dual approach, an important question to address is: why have the foreground analyses of the WMAP team not positively identified the spinning dust emission in DF07 and the haze emission in Finkbeiner (2004)?

With the MEM analysis, there are two pitfalls. First and most importantly, the MEM analysis generates a map of the spectral behavior of the soft synchrotron *in each pixel*. Since the free–free and dust spectra are kept fixed in the model, deviations away from these assumed prior spectra are absorbed into this "spectral index map" for synchrotron. Second, when minimizing $H(p)$, if the recovered model $T_m(\nu, p)$ yields negative pixel values, $\lambda(p)$ is increased until the results are greater than zero. These two effects combine so that foreground emission which does not match the prior templates and spectra (i.e., spinning dust and haze emission) are simultaneously absorbed into the synchrotron spectral index map and washed out by adding priors back into each pixel to enforce positivity. Since minimizing $H(p)$ in this way is repeated multiple times (with the synchrotron spectral index map being "updated" with each iteration) the results of the MEM analysis naturally strongly resemble the priors.

With the template fitting algorithm, the difficulty arises in the choice of a synchrotron template. Because the WMAP signal to noise ratio is far superior to previous surveys, Hinshaw et al. (2007) use the difference of the two lowest WMAP frequency maps (K−Ka) as a template for synchrotron[3]. They acknowledge that this template necessarily contains free–free emission as well, but it *also* contains the haze and spinning dust emission. Thus, the haze and spinning dust are simultaneously explicitly fit with this template. In addition, the spectra of the dust emission and free–free emission are again kept fixed so deviations are difficult to identify.

Given the numerous challenges involved in a CMB foreground analysis and the serious questions about whether all the relevant foreground emission mechanisms have even been identified yet, we choose an approach that is simple enough to have well characterized noise properties, but flexible enough to allow us to find surprises. In the limit where the spectrum of each component is invariant with position, one still has the choice of assuming a perfect spatial template, or assuming knowledge of the spectrum of each component. Given that the spectrum of each component can vary with position, neither of these approaches is strictly correct. Nevertheless, as we shall see, there is still much to be learned by making a too rigid assumption and then studying the resulting residuals.

2. METHODS

We proceed under the assumption that the morphologies of the foreground components are well characterized by external data sets and that their spectra do not vary significantly over our regions of interest (see §3.2). Thus, in principle, we should be able to find the appropriate linear combination of the foreground templates which, when combined with a CMB template, can be subtracted from the WMAP data leaving only random residuals consistent with noise.

2.1. *Template maps*

Each of the templates used in our fits has been discussed in detail by previous authors (Bennett et al. 2003; Finkbeiner 2004; Davies et al. 2006; Hinshaw et al. 2007) and so we only briefly review them here.

Free–free: Free–free (or thermal bremsstrahlung) emission originates from the Coulomb interaction of free electrons with ions in a warm gas. Since this emission is proportional to gas density squared, maps of Hα recombination line emission (which is also proportional to density squared) roughly trace the morphology of the gas and thus also the free–free emission. Our template for this foreground is the Hα map, assembled from the VTSS (Dennison et al. 1998), SHASSA (Gaustad et al. 2001), and WHAM (Haffner et al. 2003) surveys by Finkbeiner (2003). Extinction by dust (both in front of and mixed with the warm gas) presents a potential challenge in interpreting Hα as a tracer of free–free emission (Bennett et al. 2003; Finkbeiner 2004). We correct the Hα map for dust extinction using the prescription in Finkbeiner (2003), and further mitigate the effect by limiting our interest only to regions where the dust extinction is $A(H\alpha) \equiv 2.65E(B-V) < 1$ mag, where A is related to the dust optical depth $\tau_d = A/(1.086 \text{ mag})$.

The free–free spectrum is constrained by physics (Spitzer 1978; Bennett et al. 2003) as

$$T \propto \nu^{\alpha}, \quad (3)$$

where $\alpha \sim -2.15$, T is in antenna temperature, and the proportionality depends only on the electron temperature T_e. Thus the only free parameter is a scaling factor

[3] Bennett et al. (2003) used the synchrotron template described in §2.1, and an excess south of the Galactic Center is indeed visible in their residual maps (their Fig. 11, upper right panel).

equivalent to the electron temperature on the sky (but see §3), though this temperature is expected to vary with position.

Thermal and spinning dust: The emission produced from tiny interstellar dust grains vibrating in equilibrium with the surrounding radiation field has been mapped across the sky by Schlegel et al. (1998). We use their full-sky map evaluated at 94 GHz by Finkbeiner et al. (1999) (hereafter, the FDS map) as a dust template.[4] The smallest of these dust grains are expected to have a non-negligible electric dipole moment and so can also emit radiation at WMAP frequencies through rotational modes excited by collisions with ions. Thus our template also traces spinning dust emission. Since the spectral dependence of the spinning dust is not well known, we use our fit to constrain the frequency dependence of the dust-correlated foregrounds.

Soft synchrotron: As relativistic, shock accelerated electrons travel through the Galactic magnetic field, they emit synchrotron radiation with a characteristic frequency dependence $\propto \nu^{\beta}$ (in antenna temperature units). At 408 MHz, this emission was measured by Haslam et al. (1982), and we use their full-sky map as a tracer of soft synchrotron. As pointed out by Bennett et al. (2003) and Hinshaw et al. (2007) the spectral index β is expected to vary across the sky, and in particular, the spectrum may be harder near regions of recent supernova activity. Though we use our fit to evaluate the spectra of the 408 MHz-correlated synchrotron emission, we note that a value of $\beta = -3.05$ removes most of the emission at high latitude (most notably the prominent "North Galactic Spur" feature).

CMB: As we shall see in §3, the choice of CMB estimator can dramatically affect the inferred foreground spectra in a given fit. To illustrate this sensitivity, we use six different CMB estimators defined as follows.

- CMB1 – The published internal linear combination (ILC) map derived by the WMAP team for the 3-yr data.[5]

- CMB2 – An ILC with the coefficients that the WMAP team have found best cancel their Region 0 foregrounds in the three year data Hinshaw et al. (2007). This ILC is given by,

$$\begin{aligned}\mathrm{CMB2} \;=\; & 0.156\, T_{\mathrm{K}} \;-\; 0.888\, T_{\mathrm{Ka}} \;+\; 0.030\, T_{\mathrm{Q}} \\ & +\, 2.045\, T_{\mathrm{V}} \;-\; 0.342\, T_{\mathrm{W}},\end{aligned} \tag{4}$$

  where T_j is the observed WMAP temperature data in band j, in thermodynamic ΔT units.

- CMB3 – An ILC which minimizes the variance over our unmasked pixels. Here

$$\begin{aligned}\mathrm{CMB3} \;=\; & -0.032\, T_{\mathrm{K}} \;-\; 0.205\, T_{\mathrm{Ka}} \;+\; 0.037\, T_{\mathrm{Q}} \\ & +\, 0.441\, T_{\mathrm{V}} \;+\; 0.760\, T_{\mathrm{W}}.\end{aligned} \tag{5}$$

- CMB4 – A "high frequency (HF) estimator" that removes the dominant foregrounds (thermal dust and free–free) from the 94 GHz WMAP data,

$$\mathrm{CMB4} \;=\; T_{\mathrm{W}} - FDS - AH\alpha, \tag{6}$$

  where the constant A is determined from the approximate free–free amplitude at 23 GHz and traced to 94 GHz via Equation 3.

- CMB5 – A model for the thermal dust is subtracted from all of the WMAP bands using $T_{\mathrm{dust}} = (\nu/94\ \mathrm{GHz})^{1.7}\times$ FDS. A minimum variance ILC is then generated from this thermal dust pre-subtracted data (denoted by primes). The variance is minimized for,

$$\begin{aligned}\mathrm{CMB5} \;=\; & 0.104\, T'_{\mathrm{K}} \;-\; 0.289\, T'_{\mathrm{Ka}} \;-\; 0.190\, T'_{\mathrm{Q}} \\ & +\, 0.317\, T'_{\mathrm{V}} \;+\; 1.059\, T'_{\mathrm{W}},\end{aligned} \tag{7}$$

- CMB6 – A cleaned map of the 3-year data, cleaned with the Tegmark et al. (2003) (TOH) method.[6] This method utilizes a linear weighting of the data in which the weights depend on the multipole ℓ of the spherical harmonic expansion of each of the five WMAP bands.

In the limit where the noise in each WMAP band is equal to σ_0, the measurement noise of the ILC is simply

$$\sigma_L = \sigma_0 \sqrt{\sum_b \zeta_b^2} \tag{8}$$

so CMB3 and CMB5 are significantly less noisy than CMB1 and CMB2. Due to the complicated weighting of the TOH method, the measurement noise properties of CMB6 are quite complicated.

Mask: In addition to masking out all point sources listed in the WMAP team's three year catalog, as noted above, we mask all regions of the sky where the Hα extinction due to dust $A(\mathrm{H}\alpha) = 2.65E(B-V) \geq 1$ mag. We also mask out the LMC, SMC, M31, Orion-Barnard's Loop, NGC 5090, and ζ–Oph. This mask covers 21.5% of the sky.

2.2. *Fitting procedure*

Our model is that the observed WMAP data is a linear combination of the foreground templates plus the CMB[7] plus noise. Therefore, we want to solve the matrix equation

$$P\mathbf{a} = \mathbf{w}, \tag{9}$$

where $\mathbf{w}$ is the CMB-subtracted WMAP data and P is a "template matrix" whose columns consist of the foreground templates outlined in §2.1, for the coefficient vector $\mathbf{a}$ whose entries represent the weights of the individual foregrounds.

The template matrix can be represented schematically by a block-diagonal matrix,

$$P = \begin{pmatrix} P_1 & & & & \\ & P_2 & & & \\ & & P_3 & & \\ & & & P_4 & \\ & & & & P_5 \end{pmatrix}, \tag{10}$$

[4] the Hα and FDS maps can be found online at http://www.skymaps.info

[5] available at `http://lambda.gsfc.nasa.gov/`

[6] available at http://space.mit.edu/home/tegmark/wmap.html

[7] Variations in the foreground spectra from place to place on the sky will be explored by fitting smaller regions in upcoming sections

where the 5 blocks correspond to the 5 WMAP bands, and each block has the form

$$P_b = \begin{pmatrix} f_{1,b} & d_{1,b} & s_{1,b} \\ f_{2,b} & d_{2,b} & s_{2,b} \\ f_{3,b} & d_{3,b} & s_{3,b} \\ \cdot & \cdot & \cdot \\ \cdot & \cdot & \cdot \\ \cdot & \cdot & \cdot \\ f_{N_p,b} & d_{N_p,b} & s_{N_p,b} \end{pmatrix}, \tag{11}$$

where $\mathbf{f}$, $\mathbf{d}$, and $\mathbf{s}$ are the templates for free–free, thermal and spinning dust, and soft synchrotron emission (in thermodynamic mK) respectively. This makes P a $5N_p \times 15$ matrix. For each template, the mean of the unmasked pixels is subtracted, making the results of this fit insensitive to zero-point errors in the templates. For each template column, the first index represents the pixel number and the second represents a WMAP frequency band — i.e., 1=23 GHz (K), 2=33 GHz (Ka), etc. The total number of un-masked pixels in each map is N_p. For our most general fits, we assume no knowledge of the $\mathbf{f}$, $\mathbf{d}$, and $\mathbf{s}$ spectra, and so those templates do not differ for each band. Rather, we explicitly *fit* the spectra as discussed below.

The CMB-subtracted WMAP data and the coefficient vector are column vectors,

$$\mathbf{w} = \begin{pmatrix} T_{1,1} - c_1 \\ T_{2,1} - c_2 \\ T_{3,1} - c_3 \\ \cdot \\ \cdot \\ \cdot \\ T_{1,2} - c_1 \\ \cdot \\ \cdot \\ \cdot \\ T_{N_p,5} - c_{N_p} \end{pmatrix} \quad \text{and} \quad \mathbf{a} = \begin{pmatrix} a_{f,1} \\ a_{d,1} \\ a_{s,1} \\ a_{f,2} \\ a_{d,2} \\ a_{s,2} \\ \cdot \\ \cdot \\ \cdot \\ a_{s,5} \end{pmatrix}, \tag{12}$$

where $T_{i,j}$ is the observed WMAP temperature data in pixel i and band j, and $\mathbf{c}$ is one of our CMB estimators. Their lengths are $5N_p$ and 15 respectively.

Since P is not a square matrix with linearly independent rows, it is not invertible. To solve Equation 9 we calculate P^+, where $^+$ denotes the *pseudoinverse*.[8] The solution $\mathbf{a} = P^+\mathbf{w}$ minimizes the quantity $e^2 = ||P\mathbf{a} - \mathbf{w}||^2$, so that if we divide both sides of Equation 9 by the uncertainty σ (following Bennett et al. 2003 and Hinshaw et al. 2007, we use the mean measurement noise in each WMAP band), the solution[9]

$$\mathbf{a} = (P/\sigma)^+ (\mathbf{w}/\sigma) \tag{13}$$

minimizes the quantity

$$\left\| \frac{P}{\sigma}\, \mathbf{a} - \frac{\mathbf{w}}{\sigma} \right\|^2 = \frac{\|P\mathbf{a} - \mathbf{w}\|^2}{\sigma^2} \equiv \chi^2. \tag{14}$$

[8] The pseudoinverse is defined as, $P^+ = B\Sigma^+U^T$, where the singular value decomposition of $P = U\Sigma B^T$ and Σ^+ is the transpose of Σ with all non-zero singular values replaced by their inverse. In the case of a square, non-singular matrix, $P^+ \to P^{-1}$.

[9] From the properties of the pseudoinverse, $PP^+P = P$ and $[PP^+]^T = PP^+$, it is easy to show that, if the columns of P are linearly independent as they are in our case, $P^+ = [P^TP]^{-1}P^T$, making our technique equivalent to other χ^2 minimization techniques (e.g. Tegmark et al. 2003; de Oliveira-Costa & Tegmark 2006).

TABLE 1

Type	Spectra Fit Hα	Dust	Haslam	Haze†	χ^2/ν FS	GC	RG‡
1		x			3.514	6.700	4.572
2		x		x	2.993	5.147	4.213
3	x	x			3.498	6.656	4.302
4	x	x		x	2.977	5.126	4.168
5		x	x		3.506	6.650	4.241
6		x	x	x	2.988	5.106	4.169
7	x	x	x		3.489	6.611	4.208
8	x	x	x	x	2.972	5.082	4.148

NOTE. — The different types of fits performed with the procedure outlined in §2.2 using CMB5 for a CMB estimator. Fit types are characterized by which spectra are fit, and in which region of the sky: full-sky (FS), Galactic center (GC, $l, b = [-45 : +45]$), or specific regions of interest (RG, see Figure 3). † The haze template is described in §3.1. ‡ The χ^2/ν for the RG fits are averaged over all 12 regions.

This fitting procedure is flexible in that additional foreground components can be incorporated by simply adding columns to the template matrix. We will exploit this feature in §3 to model the anomalous "haze" excess emission towards the Galactic center.

The five components of each coefficient (e.g., $\mathbf{a}_{d,j}$, with j=[1:5]) represent a fit of both the amplitude and spectrum of the associated emission. By simultaneously fitting all of the spectra for all of the foregrounds, we can completely decouple the bands from each other in our fits. Additionally, we also perform less general fits in which various spectra are fixed to follow the dependencies in §2.1 (see Table 1). We point out that, fitting the spectrum of the free–free emission serves as a check on the assumption that it is well described by Equation 3 (see §3).

3. RESULTS

We have performed both full-sky fits as well as fits of smaller regions — the motivation being that both the soft synchrotron and spinning dust spectra should vary from place to place across the sky. Our fits are characterized by the χ^2 statistic of Equation 14 and by the residual map,

$$\mathbf{r} = P\mathbf{a} - \mathbf{w}, \tag{15}$$

which guides intuition and serves as a visual aid in evaluating the goodness of fit.

The fits can be separated into eight types as outlined in Table 1. The types designate which spectra are fit and whether the fit was over the full-sky (FS), the Galactic center (GC – $l, b = [-45 : +45]$), or the "regions" (RG), which were chosen as regions of interest based on $\mathbf{r}$ for a full-sky fit (see Figure 3). Also shown in Table 1 are the χ^2/ν for each fit type, where ν is the number of degrees of freedom and is given by

$$\nu = N_p - N_a, \tag{16}$$

with N_a the number of elements in the coefficient vector. Throughout the rest of this paper, we concentrate exclusively on our most general fit types 7 and 8, and unless otherwise noted, use CMB5 for a CMB estimator. This estimator is attractive both because of its uncomplicated noise properties and because the thermal dust emission has arguably the most well understood amplitude and

spectral behavior making it amenable to pre-subtraction before forming an ILC.

3.1. *Full-sky and Galactic center residual maps*

Figure 1 shows $\mathbf{r}_{\rm FS7}$ as well as the unsubtracted maps for K, Ka, and Q bands, stretched to ± 0.25, ± 0.12, and ± 0.08 mK respectively. The fit yields $\chi^2_{\rm FS7}/\nu = 3.49$, removing 95.8%, 95.7%, 96.3%, 97.5%, and 99.7% (for K, Ka, Q, V, and W[10] bands respectively) of the variance from the WMAP data. However, it is clear from the second row of Figure 1 that there is still a remaining emission residual towards the Galactic center (GC). This residual is the "haze" present in the 1 year data as shown by Finkbeiner (2004).

Although the average power in the haze is small (with a mean of just 0.59 kJy/sr per pixel at 23 GHz within 30 degrees of the GC in the southern sky), our fit may be compensating for its presence by adjusting the weights of the other foreground templates. To relax the stress on the fit, we adopt a crude model for the haze emission,

$$\mathbf{h} \propto \begin{cases} \frac{1}{r} - \frac{1}{r_0} & \text{for } r < r_0; \\ 0 & \text{for } r > r_0, \end{cases} \tag{17}$$

where r is the distance to the Galactic center and we arbitrarily set $r_0 = 45$ degrees. Since the emission mechanism is unknown, we fit the spectrum of the haze as well. The extent to which the other fit parameters change gives an idea of the cross talk between the haze and the other templates.

The third row of Figure 1 shows residual maps for FS8. It is clear from $\mathbf{r}_{\rm FS8}$ alone that the fit is improved, particularly in the southern GC where obscuration from dust and gas is minimal and in the high latitude north where the North Galactic Spur synchrotron feature is no longer over subtracted at 23 GHz (compare rows 2 and 3 of Figure 1). Though $\chi^2/\nu_{\rm FS8} = 2.97$ is only slightly lower than the FS7 fit, we emphasize that the number of degrees of freedom is quite large ($\nu \sim 155,000$) and so the likelihood for the FS8 model is significantly higher. Furthermore, we are including many pixels at large Galactic latitudes where the signal to noise is very low and the amplitude of the haze is very small.

Since the ISM may have different properties near the GC (i.e., lower gas temperature due to more efficient cooling because of higher metallicity, increased supernova activity, etc.), it is instructive to consider this region separately from the rest of the sky. Figure 2 shows $\mathbf{r}$ maps for the GC7 and GC8 fits. There is a significant decrease in χ^2/ν from GC7 to GC8 with the inclusion of our haze template — from 6.61 for GC7 to 5.08 for GC8. The substantially oversubtracted regions near the edge of the mask in $\mathbf{r}_{\rm GC7}$ indicate that the fit is indeed attempting to compensate for the haze by adjusting the amplitudes of other templates. Although there is still some over subtraction in $\mathbf{r}_{\rm GC8}$, the overall quality of the fit is much improved, particularly in the southern sky.

In the *northern* sky, there is a large structure just north-west of the GC in and around the region of Rho-Oph. Typically, extended regions of over- or under-subtraction in our fits are indicative of variations in the physical conditions of the emission media. However, in this circumstance, it is unclear if the under-subtraction is due to an over simplification of the radial haze profile given our template for this component (Equation 17). The next step is to subdivide the sky into certain regions of interest where our fit is the least successful and fit those regions explicitly.

[10] The noise in W band is especially low because the coefficient of T_W in the CMB5 estimator is very close to one, so the CMB-subtracted W band data has essentially no W band data in it. Therefore results from W band should be viewed with suspicion.

3.2. *Regional fits and composite maps*

Our regions of interest were identified as regions of particularly notable over- or under-subtraction in $\mathbf{r}_{FS8}$. Figure 3 shows the boundaries of these regions superimposed on the raw WMAP data at 23 GHz, $\mathbf{r}_{\rm FS8}$, as well as a composite map for $\mathbf{r}_{\rm RG8}$ (a fit which includes our haze template). The residual map (which is actually the residual maps of each region stitched together with *no* smoothing) is shown for both RG8 and RG7 fits in Figure 4 (the maps stretched to the same units as Figure 1).

At all frequencies, the RG8 fit more effectively removes the foregrounds than the RG7 fit. There are more regions of over-subtraction in $\mathbf{r}_{\rm RG7}$ (both at high latitudes and around the mask edges) compared to $\mathbf{r}_{\rm RG8}$, the region boundaries are somewhat less continuous in $\mathbf{r}_{\rm RG7}$, and most importantly, the haze is *still* present in the $\mathbf{r}_{\rm RG7}$ maps. These composite $\mathbf{r}$ maps are completely unsmoothed and it is a testament to the quality of our RG8 fit that there are no discernible large scale brightness gradients between adjacent regions.

Lastly, we define the residual haze map

$$\mathbf{r}_H = \mathbf{r}_{\rm RG8} + \mathbf{a}_h \mathbf{h}, \tag{18}$$

where the appropriate amount of haze is added back in to each region (i.e., the same amount as was subtracted by the fit). The bottom row of Figure 4 shows $\mathbf{r}_H$. Despite the fact that the haze fit coefficients are not constrained to be continuous across the region boundaries, $\mathbf{r}_H$ has no clear discontinuities.

3.3. *Foreground spectra*

Figure 5 shows the FS8 spectra (coefficient vectors) in kJy/sr per template unit: Rayleighs for Hα, mK for FDS and Haslam, and arbitrary units for the haze. The most striking feature of these spectra are that they are very sensitively dependent on the estimator used for the CMB. For example, the synchrotron spectrum actually appears to turn *up* at high frequencies for CMB1, CMB2, and CMB3, while CMB4 and CMB5 give the more physically motivated power law type spectra. This dependence is entirely due to the contamination of the CMB by foregrounds, which can never fully be removed for any CMB estimator. Thus, when we remove the estimator from the WMAP data to perform the foreground fit, we have inadvertently added (or subtracted) some foregrounds from the data with essentially the spectrum of the CMB ($I_\nu \propto \nu^2$). We emphasize that the contamination is small, so that it has minimal effect on the *variance* of the CMB estimator, but it is large compared to the relative amplitudes of the foregrounds. This is especially true for estimators which minimize the variance of an ILC; in this case the contamination is proportional to the cross correlation of the true CMB with the true foregrounds (see §4).

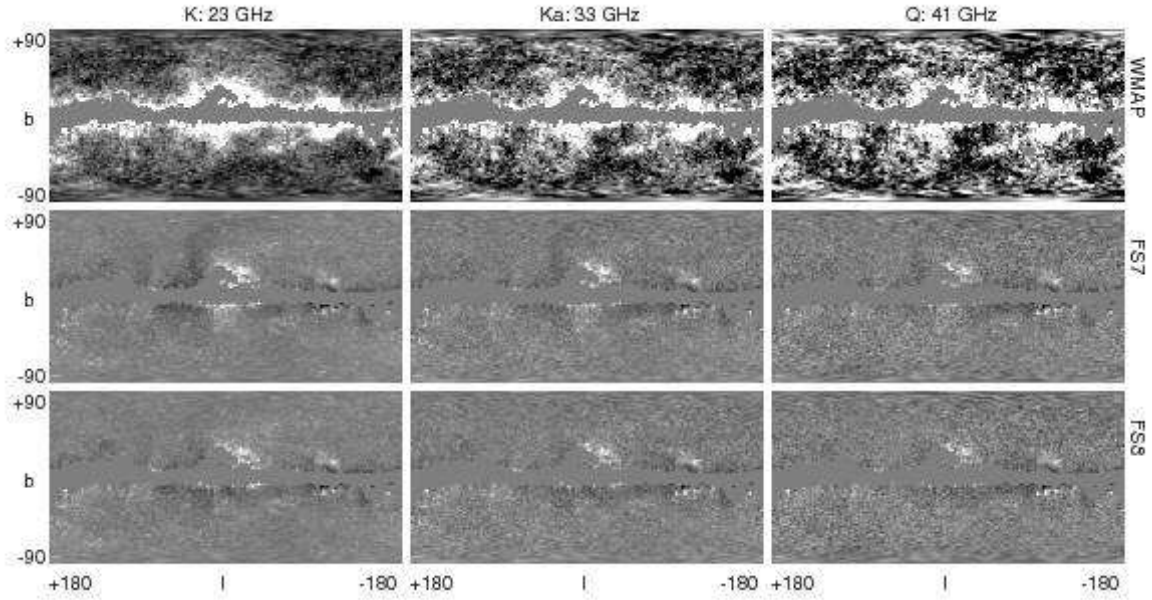

FIG. 1.— Residual maps **r** for three of the five bands and for FS7 and FS8 fits using CMB5 (the K, Ka, and Q band maps are stretched to ±0.25, ±0.12, and ±0.08 mK respectively; all maps are mean subtracted). The unsubtracted WMAP data are also shown for comparison. The FS7 fit removes much of the emission, however there is a remaining excess towards the Galactic center. This excess emission is particularly notable south of the Galactic center where obscuration by dust and gas is negligible. FS8 incorporates a simple spatial template for this haze and removes much of the residuals in that region.

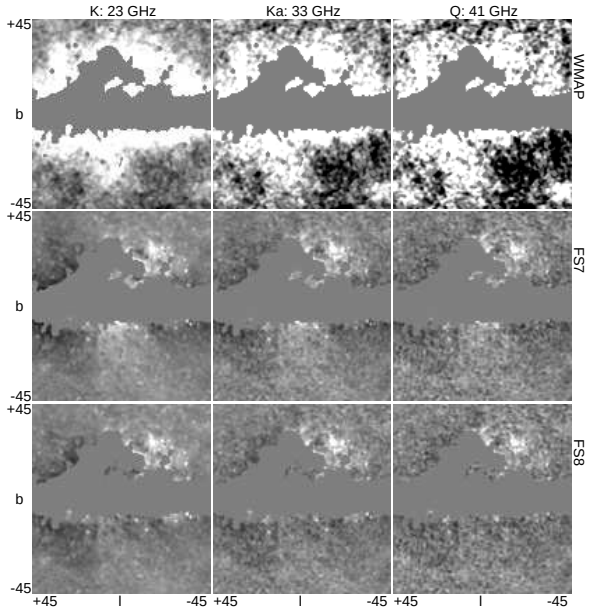

FIG. 2.— The same as Figure 1 except for the GC fits ($l, b = [-45 : 45]$ degrees). Though GC7 explicitly fits the free–free, dust, *and* synchrotron spectra, the haze is still present in $\mathbf{r}_{\rm GC7}$ indicating that it is morphologically dissimilar to the those templates. The quality of the fit is substantially improved with the inclusion of a haze template (GC8). The extended structure in the north-west GC is likely due to an imperfect haze template.

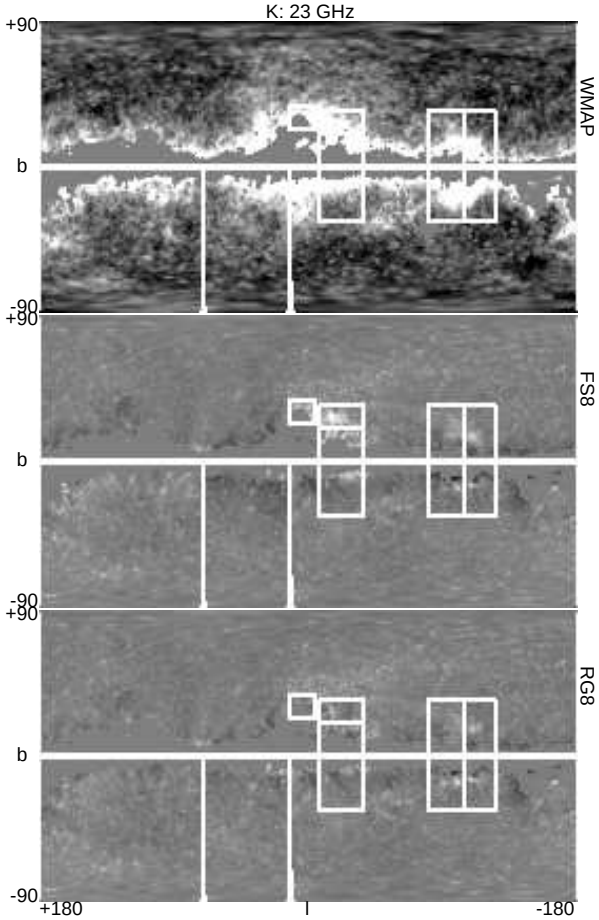

FIG. 3.— Illustration of the 12 regions independently fit in the RG fits. Breaking the sky up in this way removes many of the over- and under-subtracted features in the residual maps, particularly the excess emission in the north-west GC.

Despite the large uncertainties, there are concrete conclusions that can be drawn from Figure 5. First, the Hα-correlated emission does *not* follow the $I_\nu \propto \nu^{-0.15}$ frequency dependence as expected. Instead there is a bump in the spectrum around 30 GHz. In our companion paper (Dobler & Finkbeiner 2007) we argue that the Hα-correlated emission has a spectrum that is consistent with a classical $\nu^{-0.15}$ spectrum plus a WIM spinning

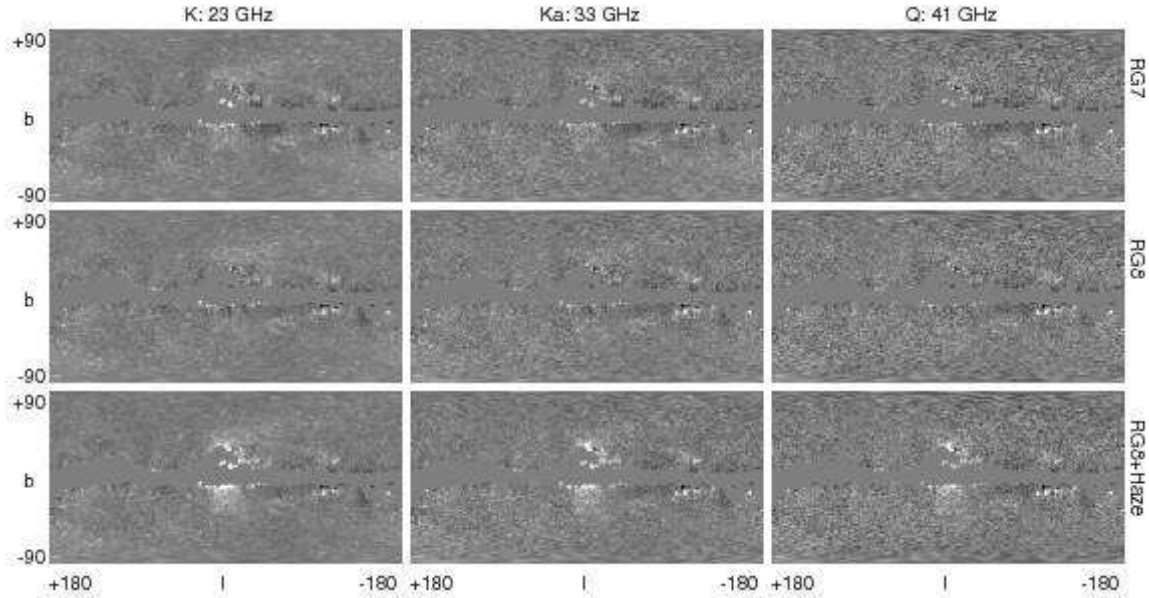

FIG. 4.— Residual maps for the RG7 and RG8 fits using CMB5, with the same stretch as Figure 1. The haze is still present in the $\mathbf{r}_{\rm RG7}$ fits despite the relatively small size of the fitting regions. The bottom row shows $\mathbf{r}_{\rm RG8}$ with the subtracted haze in each region added back in to that region. These maps are unsmoothed and no continuity constraints are placed on the region boundaries.

dust component. Second, although the soft synchrotron and haze spectra vary substantially with CMB estimator type, for a given type, the haze is always *harder* than the normal soft synchrotron, a point which we explore in more detail below.

Finally, like Bennett et al. (2003), Finkbeiner (2004), Davies et al. (2006), and Hinshaw et al. (2007), we find that the dust-correlated emission falls from 94 to 61 GHz but then rises to 23 GHz consistent with emission from both thermal and spinning dust. Since these spectra are the result of fits over large areas of the sky and the spinning dust spectrum is expected to vary with position, it is not surprising that we do not see a peak in the dust-correlated emission in the range 20-40 GHz as in the Draine & Lazarian (1998b) models. Rather, we are seeing a superposition of many spinning dust spectra with varying peak frequencies. This has led to the misidentification of the this dust-correlated emission as synchrotron in the past (Bennett et al. 2003; Hinshaw et al. 2007).

It is tempting to conclude that the RG fits for the individual regions can be used to construct a map of the variation in the spinning dust spectra across the sky. Such a map would represent an "excitation map" or "irradiation map" for the dust grains. However, this is simply not possible given the contamination of the CMB estimator by the foregrounds.[11]

3.4. *Comparison of the haze and soft synchrotron*

From Figure 5 it seems that the haze spectrum is inconsistent with a $\nu^{-0.15}$ free–free spectrum. While some of the CMB estimators do yield such hard spectra at low frequencies, those fits turn up at high frequencies. This behavior is *much* less likely than simply a contamination of the CMB estimator by the haze emission. Furthermore, the haze is most clearly visible in the southern GC where dust obscuration is minimal so that the haze should either show up in the Hα map (if it is $T < 10^5$ K gas) or in the ROSAT X-ray data (if it is $T > 10^6$ K gas). Since neither of these is the case, and since gas at intermediate temperatures is thermally unstable (see Spitzer 1978), we concluded that the most likely source of the haze is synchrotron emission from relativistic electrons. Figure 5 also shows that this synchrotron emission is harder than the soft synchrotron traced by the Haslam 408 MHz map.[12]

Figure 6 shows density contours for a scatter plot of the unmasked pixel values in $\mathbf{r}_H$ and the total synchrotron residual map, $\mathbf{r}_{H+S} = \mathbf{r}_H + \mathbf{a}_s\mathbf{s}$, in antenna temperature for various frequency combinations. The pixels shown have $l = [-25 : +25]$ and $b = [-45 : 0]$. Despite the large scatter, the $\mathbf{r}_H$ emission appears to be a distinctly separate component of synchrotron emission with a spectral index that is significantly harder than the synchrotron (as shown in Table 2 this behavior persists for all CMB estimator types, though the precise spectral indices are very uncertain due to the CMB estimator bias describe in §4). This point is underscored in an RGB color coded map of the 23, 33, and 41 GHz $\mathbf{r}_H$ and $\mathbf{r}_S$ maps. The haze emission is distinctly bluer (harder spectral index) than the total, redder (softer) synchrotron emission in the Galactic center.

Figure 8 shows the total intensity of the haze as a function of distance south of the Galactic center. The radial bins are 20 degrees wide and separated by 1 degree in latitude. Our simple $1/r$ profile for the haze emission is

[11] Uncertain zero point variation across the maps (due to instrumental limitations, imperfect zodiacal light subtraction, etc.) is also a consideration, but it is subdominant.

[12] In their first and third year temperature analysis, the WMAP team concludes that the spectrum of the *soft* synchrotron is harder near the Galactic plane and particularly near the Galactic center (Bennett et al. 2003; Hinshaw et al. 2007). This may be inconsistent with Page et al. (2007) and Kogut et al. (2007) who find a more or less constant synchrotron spectral index across the sky from the WMAP polarization data. Given the difficulties in the interpretation of the MEM analysis (see §1.3), the reason for the discrepancy is unclear.

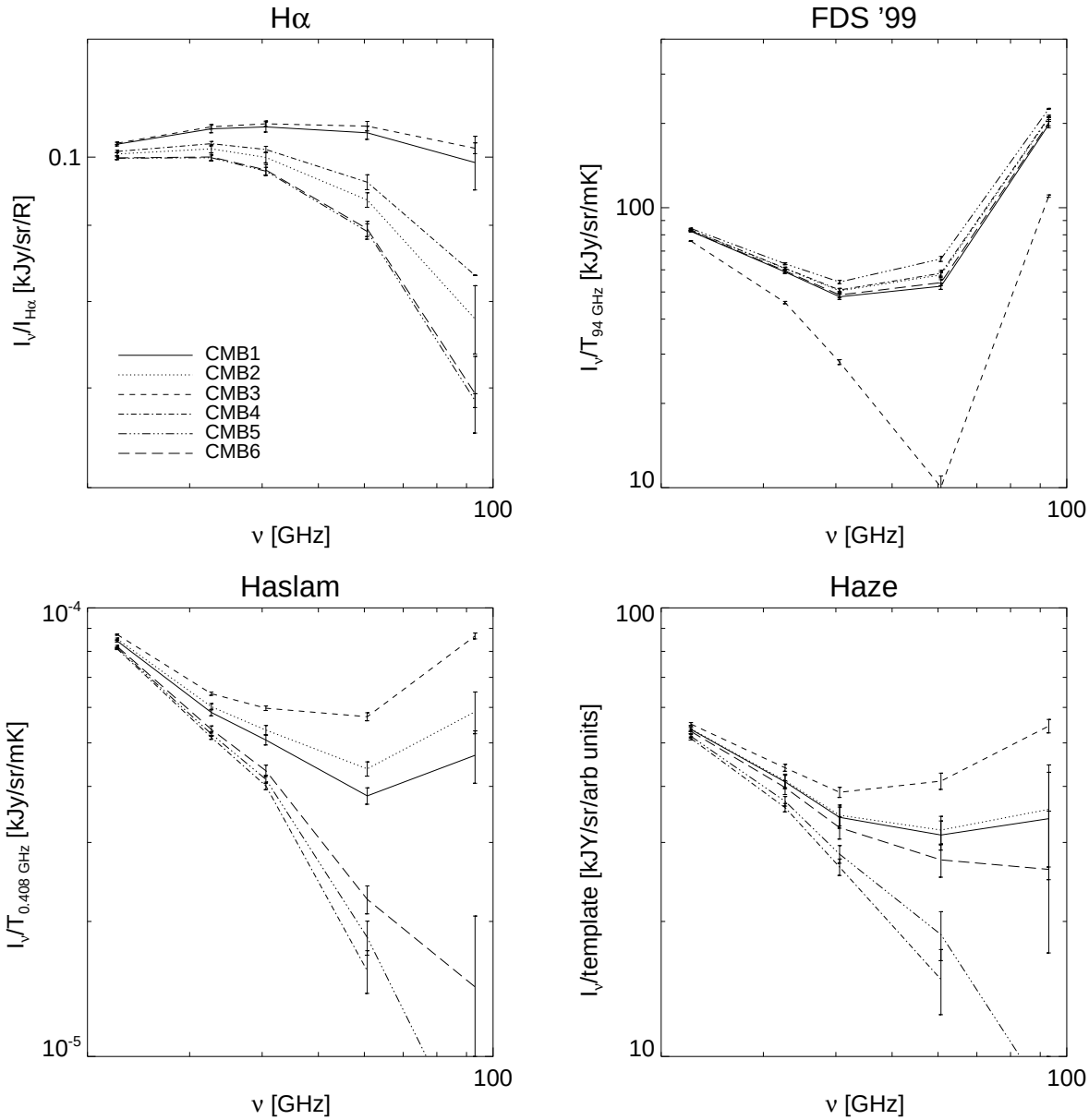

FIG. 5.— Foreground spectra for the FS8 fits with our six CMB estimators: solid = CMB1, dotted = CMB2, short dashed = CMB3, dot-dashed = CMB4, dot-dot-dot-dashed = CMB5, and long dashed = CMB6. The error bars on the coefficients are the formal error bars on the fit (see text).

TABLE 2

CMB estimator	β_S 23/33	β_S 33/41	β_S 23/41	β_H 23/33	β_H 33/41	β_H 23/41
1	-2.86	-2.58	-2.81	-2.14	-2.13	-2.23
2	-2.78	-2.47	-2.71	-1.98	-1.98	-2.01
3	-2.75	-2.53	-2.66	-2.24	-2.56	-2.31
4	-3.15	-3.33	-3.22	-2.57	-3.14	-2.76
5	-3.10	-3.13	-3.15	-2.39	-2.67	-2.52
6	-3.00	-3.05	-3.01	-2.37	-2.92	-2.51

NOTE. — The best fit spectral slopes for $\mathbf{r}_{H+S}$ (β_S) and $\mathbf{r}_H$ (β_H) maps for the RG8 fits at 23, 33, and 41 GHz over unmasked pixels (with $l = [-25 : +25]$ and $b = [-45 : 0]$, see Figure 6). Though there is significant scatter in the inferred spectral index, the haze residual is always *harder* than the total synchrotron signal.

not adequately describing the structure of the haze — which is also clear from the residual maps in Figures 1 and 2. Furthermore, the systematic error bars due to chance correlation between the haze and the CMB are quite large, particularly at high frequencies.

4. CMB ESTIMATOR BIAS

While the statistical uncertainty in our fits comes from measurement noise in the WMAP data, systematic uncertainties in our fits are dominated by contamination of the CMB estimator by the foreground components. We have used six different CMB estimators, but they can be separated into two categories: ILC type estimators in which multiple WMAP bands are combined to approximately cancel the foregrounds (CMB1, CMB2, CMB3, and CMB5), and HF estimators in which a model for the thermal dust and free–free emission is removed from the

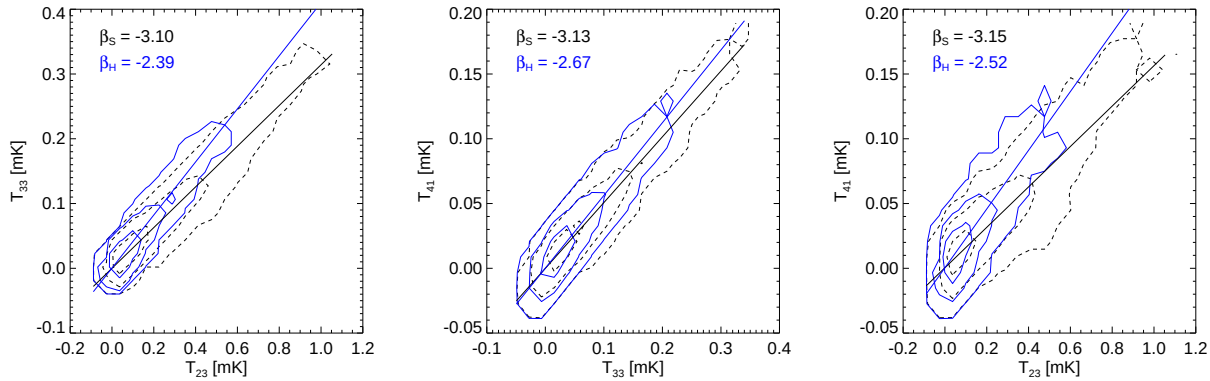

FIG. 6.— Number density contours of unmasked pixel (with $l = [-25 : +25]$ and $b = [-45 : 0]$) temperatures in the $\mathbf{r}_H$ (blue) and $\mathbf{r}_{H+S}$ (dashed) maps for the RG8 fits at 23, 33, and 41 GHz for CMB5. Though the spectral slope is somewhat uncertain between each band and can vary significantly depending on which CMB estimator is used (see Table 2), the best fit spectral slope for the haze emission is distinctly harder than for the total synchrotron.

highest WMAP band to approximately leave the CMB (CMB4).

4.1. *ILC estimators*

Hinshaw et al. (2007) point out that the WMAP data consists of the "true" CMB, T_c plus some additional contamination by foreground components T_j which have some spectral dependence $N_{i,j}$ where i and j represent the observing band and foreground component respectively. That is,

$$W_i = T_c + \sum_j N_{i,j} T_j \tag{19}$$

so that an internal linear combination of the WMAP bands is,

$$\begin{aligned} L &= \textstyle\sum_i \zeta_i W_i \\ &= \textstyle\sum_i \zeta_i T_c + \sum_{j,i} \zeta_i N_{i,j} T_j \\ &= T_c + \textstyle\sum_j \Gamma_j T_j, \end{aligned} \tag{20}$$

where ζ_i are constrained to sum to one in order to preserve unity response to the CMB, and Γ_j parameterizes the contamination of L by foreground j.

Let us consider that there are four types of foreground emission: free–free (F), dust (D), soft synchrotron (S), and the haze (H). Each of these has an associated Γ, and so the ILC is given by

$$L = T_c + \Gamma_F T_F + \Gamma_D T_D + \Gamma_S T_S + \Gamma_H T_H. \tag{21}$$

Since ζ_i are chosen to minimize the variance in L,

$$\frac{\partial \langle L^2 \rangle}{\partial \Gamma_j} = 0 \tag{22}$$

for all j, and we have explicitly assumed mean subtracted maps so that $\langle L \rangle = \langle T_c \rangle = \langle T_j \rangle = 0$. Now,

$$\begin{aligned} L^2 &= T_c^2 + 2 \textstyle\sum_j \Gamma_j T_c T_j \\ &\quad + 2 \textstyle\sum_j \sum_{k \neq j} \Gamma_j \Gamma_k T_k T_j \\ &\quad + \textstyle\sum_j \Gamma_j^2 T_j^2 \end{aligned} \tag{23}$$

so that Equation 22 reads

$$0 = 2\langle T_c T_j \rangle + 2 \sum_{k \neq j} \Gamma_k \langle T_j T_k \rangle + 2\Gamma_j \langle T_j^2 \rangle. \tag{24}$$

(note: the notation in Equation 24 can be compactified into $0 = \sum_\psi \Gamma_\psi \langle T_j T_\psi \rangle$ where $\psi = [c, F, D, S, H]$ and $\Gamma_c \equiv 1$) Thus, we can solve explicitly for

$$\Gamma_j = -\frac{\langle T_c T_j \rangle + \sum_{k \neq j} \Gamma_k \langle T_j T_k \rangle}{\langle T_j^2 \rangle} \tag{25}$$

In the limit of only one foreground T_f the second term (which represents cross correlation between the different foreground morphologies) disappears and this reduces to $\Gamma = \Gamma(T_c, T_f) = -\sigma_{cf}/\sigma_f^2$ as derived with a similar method by Hinshaw et al (2006).

According to Equation 25, the ILC map is biased towards anti-correlation between different "true" foreground emission morphologies and the "true" CMB. However, since we do not know the true T_c or T_j *a priori*, we have no information about how much of each foreground to add back into L in order to correct for this factor.

We can use Monte Carlo techniques to estimate the amplitude (but *not* the sign) of the error in L due to foreground contamination as follows. We construct 100 realizations of the CMB by generating random phases for the measured power, C_ℓ, in each Fourier mode of the binned three year WMAP power spectrum ($\ell_{\max} = 986$) from Spergel et al. (2007). For each realization T_c' we can estimate Γ with a reasonable foreground template T_j' which we suppose traces the morphology of the emission (see §2.1).

Figure 9 shows histograms of

$$\Gamma' \sigma_j = \Gamma(T_c', T_j') \sigma_j, \tag{26}$$

where σ_j is the standard deviation over unmasked pixels of the foreground template T_j' ($T_j' =$ Hα, FDS, Haslam, and haze), for all 100 realizations of the CMB sky. We multiply by σ_j to obtain the contamination in a "typical" pixel in the ILC map. Each histogram has a mean consistent with zero,

$$\langle \Gamma' \rangle \approx 0 \text{ for each } T_j' \tag{27}$$

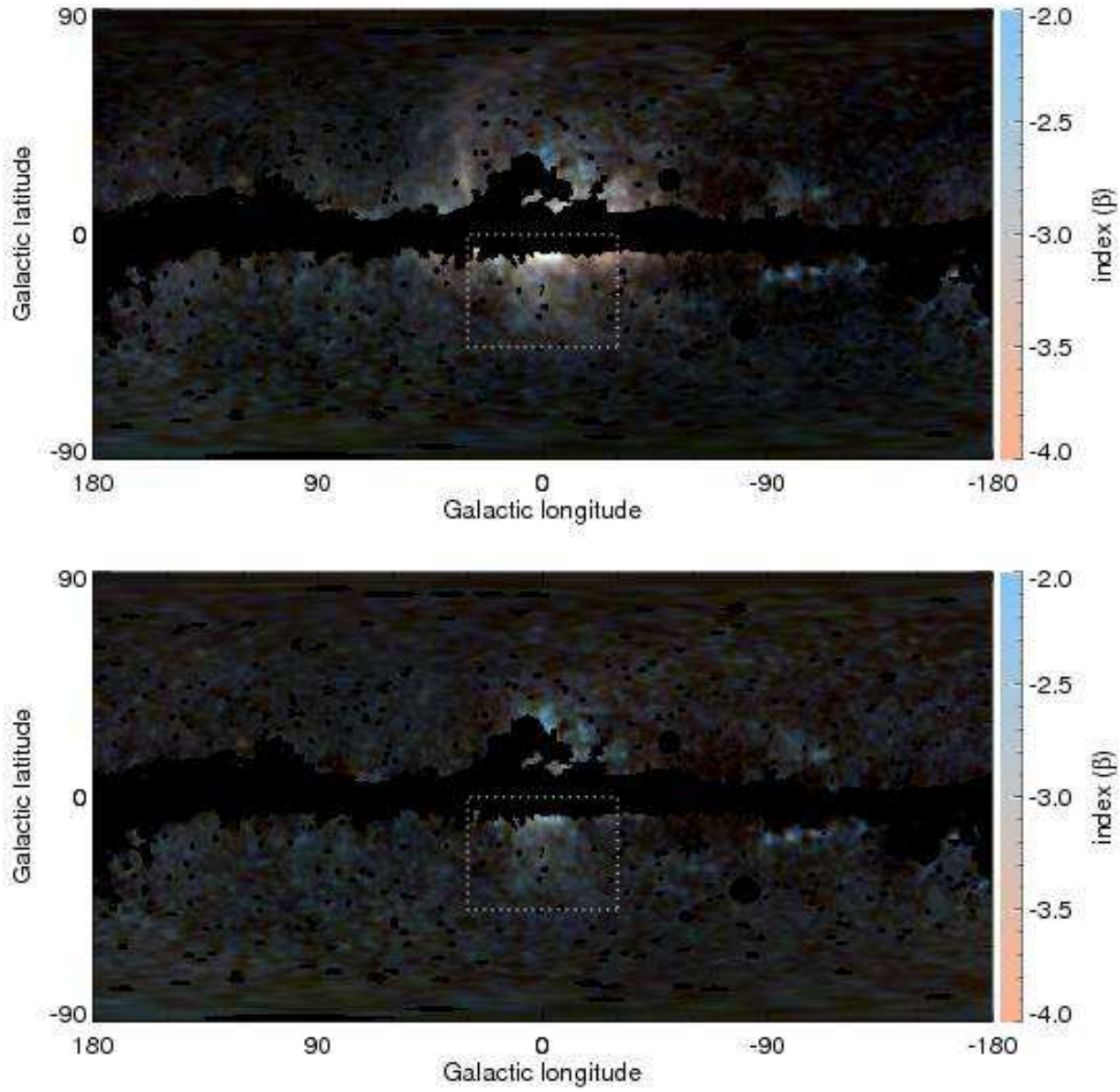

FIG. 7.— An RGB representation of $\mathbf{r}_H$ and $\mathbf{r}_{H+S}$ for RG8 with CMB5. The color coding indicates the spectral index, in antenna temperature, of a given pixel. In particular, the bluer haze region (*box*) indicates a harder spectrum than the redder synchrotron emission.

as expected since the CMB realization T_c' is just as likely as $-T_c'$. The implication is that we can only estimate the *uncertainty* in $T_{\rm ILC}$, we cannot explicitly correct for the bias.

It is important to note that, although L cannot be corrected for the cross-correlation bias, the net effect is to *decrease* the variance relative to the true CMB, T_c. Since the bias of the variance is not mean zero, the effect on the power spectrum of the CMB can be estimated (cf. Hinshaw et al. 2007).

4.2. *HF type estimators*

The bias in a HF estimator is easy to understand and due entirely to the residual foreground emission after subtraction of thermal dust and free–free. Assuming perfect subtraction of these two foregrounds, whatever other foregrounds are left in the HF estimator are subtracted off all lower frequency bands leading to a systematic bias towards softer spectra for the soft synchrotron and haze components.

4.3. *Forecasts for* Planck

The principle advantage of the *Planck* mission over WMAP is the large range of frequency coverage. In particular, the multiple channels at very high frequency reduce the foreground problem to (mostly) a single emission mechanism, thermal dust. In order to exploit this feature, we suggest a new approach based on an ILC type CMB estimator. However, instead of minimizing the variance (which we have seen leads to large cross-correlation uncertainties), we choose the ILC coefficients ζ_i to cancel as many *power law* foreground components as possible. This estimator can then be subtracted off of lower frequency bands with very minimal bias contami-

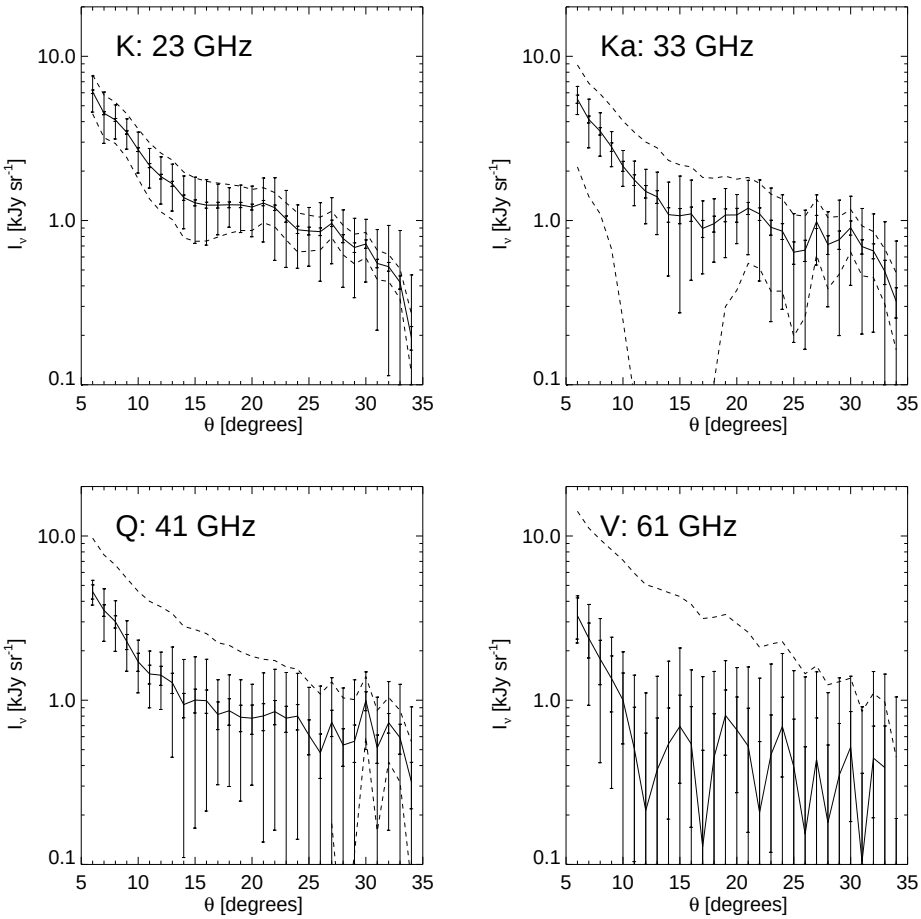

FIG. 8.— Integrated haze (from the bottom panel of Figure 4) in kJy/sr as a function of radial distance south of the Galactic center. The radial bins are 20 degrees wide and separated by 1 degree in longitude. The inner error bars are due to the formal error on the fit coefficients, the outer error bars are the 1-σ standard deviation of the temperature fluctuations in a given radial bin, and the dotted lines represent the bias due to chance correlation between the CMB and the haze.

nation of the inferred foreground spectra

Planck's frequency coverage is 30, 44, 70, 100, 143, 217, 353, 545, and 857 GHz. If we estimate that spinning dust emission is negligible above 100 GHz, then these bands contain mostly thermal dust ($T \propto \nu^{\beta_+}$ with $1.6 \leq \beta_+ \leq 2.3$) and also small amounts of free–free, synchrotron, and haze ($T \propto \nu^{\beta_-}$ with $-3.1 \leq \beta_- \leq -2.1$).

In order to find an ILC that optimally cancels out this range of power law indices, we formulate the error function,

$$\delta_{94}(\beta) = \frac{T_{94}}{\sum_i \zeta_i T_i}, \tag{28}$$

for a foreground spectrum, normalized to 94 GHz, $T_i = T_{94}(\nu_i/94\ \mathrm{GHz})^\beta$, where ν_i are the *Planck* bands above 100 GHz and the sum is over bands. The physical interpretation of $\delta_{94}(\beta)$ is that it represents the fractional bias in the inferred 94 GHz amplitude of a foreground with power law index β. We minimize $\int \delta_{94}^2 d\beta$ with respect to ζ_i over the range β_+ and β_- defined above. Figure 10 shows the resultant δ_{94}. With these ζ_i we can form the *Planck* ILC $L_\mathrm{P} = \sum_i \zeta_i P_i$, where P_i are the *Planck* data in thermodynamic mK at band i. We find that

$$\begin{aligned} L_\mathrm{P} = &-1.49P_{143} + 3.21P_{217} - 0.74P_{353} \\ &+0.02P_{545} - 3.21\times10^{-5}P_{857} \end{aligned} \tag{29}$$

minimizes the area under the δ_{94}^2 curve over the β range of interest. Using only the high frequency channels in this way avoids ambiguities due to an uncertain spinning dust spectrum.

To estimate the contamination of L_P by synchrotron and haze emission we must make a couple of assumptions. First, let us assume that these foregrounds follow a power law with with amplitudes of roughly our fit results at 23 GHz from Figure 5 and indices $-3.1 \leq \beta_S \leq -2.7$ and $-2.7 \leq \beta_H \leq -2.4$ respectively. Second, we make the implicit approximation that the morphologies of the foreground emission mechanisms do not change with frequency and that they are still well represented by the templates in §2.1.

Figure 10 shows our estimates for the error bars on the "mock true" soft synchrotron and haze spectra at WMAP frequencies given three CMB estimators: a WMAP only ILC (leading to cross correlation bias errors), our WMAP HF estimator CMB4, and the L_P estimator. As we have already seen, the WMAP only ILC clearly yields very large uncertainties, though they have the advantage of being mean zero (averaged over an ensemble of CMB realizations). CMB4 does significantly better, though now the errors are systematically biased towards softer spectra. With L_P, the bias errors are al-

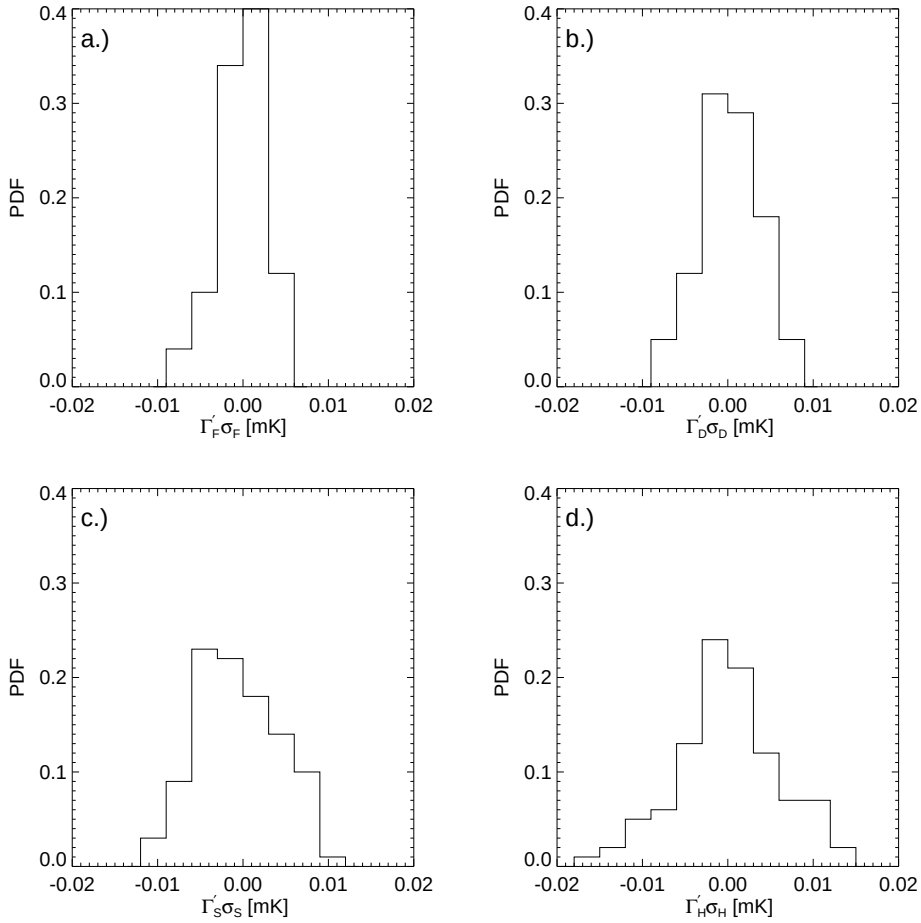

FIG. 9.— Distribution of ILC chance cross correlation biases for 100 realizations of the CMB sky. a.) Hα-correlated emission, b.) dust-correlated emission, c.) Haslam-correlated emission, and d.) haze emission.

most completely eliminated. For a foreground with indices β = -3.1, -2.7, and -2.4, the bias errors at 23 (94) GHz are -0.11%, -0.06%, and $+0.13\%$ (-7.6%, -2.2%, and $+3.3\%$) respectively.

We emphasize that we have by no means attempted to formulate the "optimal" foreground removal algorithm for *Planck*. There have been numerous discussions on the topic describing and comparing different cleaning methods.[13] Rather, we have demonstrated that, by exploiting the many bands and high frequency coverage, this simple *Planck* ILC will substantially reduce the systematic biases in the inferred foreground spectra compared to WMAP.

5. DISCUSSION

We have carried out a multi-linear regression fit to the WMAP data using foreground templates for free–free, soft synchrotron, and dust emission. We perform fits over both the (nearly) full-sky as well as smaller regions of interest. Our method simultaneously fits the amplitude and spectrum of each emission component and is immune to priors or initial "guesses" for the template amplitudes.

Importantly, we find that the spectra of the foreground emission mechanisms cannot be determined to high accuracy with the WMAP data. The root cause is that any estimator of the CMB will necessarily be contaminated by the foregrounds to some degree, so that subtracting the CMB estimator from the WMAP data systematically biases the inferred foreground spectra. Thus, the fit spectrum for each foreground is contaminated by some amount of CMB spectrum. The degree of systematic bias in the foreground spectra can be quite large and varies dramatically among our different CMB estimators. It is worth noting that the degree of contamination of a given CMB estimator does not significantly affect the variance of the estimator.

We find that, upon removing the free–free, dust, and soft synchrotron emission, the 3–year WMAP data still contains the "haze" seen by Finkbeiner (2004). Since this haze emission is present in all residual maps regardless of which CMB estimator is used, we conclude that it is not an artifact of imperfect CMB subtraction. We have included a simple $1/r$ template for the haze to relax the stress on the other foreground components in our fit. This template imperfectly matches the morphology of the

[13] E.g., Brandt et al. (1994) undertook an early study of foreground removal with multiple frequency bands, Tegmark et al. (2003) and de Oliveira-Costa & Tegmark (2006) describe an ILC type method in which the weighting depends on the multipole ℓ of the spherical harmonic decompostion, Barreiro et al. (2004) expands on the MEM analysis, Eriksen et al. (2006) describe a component separation method, Hansen et al. (2006) tackle the problem with a wavelet analysis, and Dodelson (1997) attempts to "design" an experiment with optimal frequency coverage for removing foregrounds.

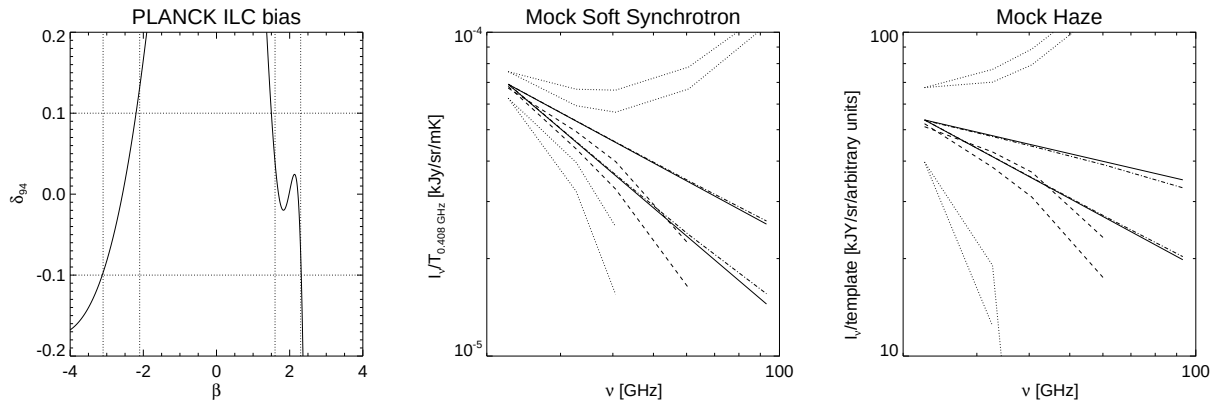

FIG. 10.— Left panel: fractional error in the inferred 94 GHz amplitude of a foreground with $T \propto \nu^{\beta}$ due to contamination of the *Planck* ILC $L_{\rm P}$ (see Equation 29). Center and right panels: biases due to foreground contamination of different CMB estimators for mock soft synchrotron ($T_S \propto \nu^{\beta_S}$ with $-3.1 \leq \beta_S \leq -2.7$) and the haze ($T_H \propto \nu^{\beta_H}$ with $-2.7 \leq \beta_H \leq -2.4$). The mock spectrum is shown with a solid line. The dotted lines are the mean zero ILC bias errors using only WMAP data alone, the dashed lines are the systematic biases due to CMB4, and the dot-dashed lines are the systematic bias using $L_{\rm P}$. The systematic biases with *Planck* are more than an order of magnitude smaller than for a WMAP HF estimator.

haze, but allows us to simultaneously fit an approximate amplitude and spectra of the haze emission as well.

Despite the above issue of bias errors, we can make the following concrete statements about our fit foreground spectra.

1. We find that the Hα-correlated emission does not follow a simple $I_\nu \propto \nu^{-0.15}$ free–free powerlaw as expected from theory. Rather we find a bump in the Hα-correlated emission which we argue in our companion paper D+F (2007) can be explained by a mixture of free–free gas and spinning dust. We emphasize that this bump is *not* due to the contamination of the CMB estimator by the foregrounds.

2. The dust-correlated emission has the now familiar fall off from 23 to 41 GHz consistent with a superposition of D+L spinning dust spectra and then a rise at 94 GHz from thermal dust emission. We cannot use our multi-region fits to map out variations in the spinning dust spectrum from place to place across the sky since the uncertainty from the systematic bias dominates.

3. Our soft synchrotron spectra are very sensitively dependent on which CMB estimator is used. For example, with the WMAP team's published ILC, the soft synchrotron spectrum actually turns up at high frequencies, while other estimators show a steadily falling spectrum (with $T_\nu \propto \nu^{\beta}$ where $\beta \approx -3.0$.) This ambiguity is entirely due to the contamination of the CMB estimator by soft synchrotron type emission.

4. The haze spectrum is similarly very uncertain due to CMB estimator bias, however, for a given estimator, the haze spectrum is always harder than the soft synchrotron. For reasons outlined in §3.4, we suspect that the haze emission is due to hard synchrotron from a separate component of very energetic electrons near the Galactic center. Possible sources include products of dark matter annihilation (Hooper et al. 2007) or a single energetic event in the last million years, e.g. a gamma-ray burst (Broderick et al. 2007).

Upcoming experiments like *Planck* will significantly reduce the problem of CMB estimator bias in the inferred foreground spectra due to the improved high frequency coverage. In particular, for frequencies $\nu > 100$ GHz the *Planck* data will be virtually free of all foregrounds except for thermal dust. Removing this one bright component with five bands is significantly less ambiguous than removing three or four bright components with five bands. Furthermore, what little free–free, soft synchrotron, and haze emission there is at these high frequencies can be roughly eliminated in a *Planck* CMB estimator through the appropriate choice of ILC coefficients. We estimate that the systematic uncertainties in soft synchrotron and haze spectra will be reduced by more than an order of magnitude compared to WMAP.

Galactic foreground emission represents the most significant contaminant in determining cosmological parameters. Ironically, the reverse statement is also true and in order to make progress towards determining the "true" spectra of the foreground emission, a more reliable estimate of the CMB sky is required.

We thank Gary Hinshaw, Angelica de Oliveira-Costa, Max Tegmark, and the anonymous referee for helpful comments and suggestions. Some of the results in this paper were derived using HEALPix (Górski et al. 1999; Calabretta & Roukema 2007). This research made use of the NASA Astrophysics Data System (ADS) and the IDL Astronomy User's Library at Goddard[14]. DPF and GD are supported in part by NASA LTSA grant NAG5-12972.

[14] Available at `http://idlastro.gsfc.nasa.gov`

REFERENCES

Barreiro R.B. et al., 2004, MNRAS, 351, 515
Bennett C.L. et al., 2003, ApJS, 148, 97
Boughn S.P. & Pober J.C., 2007, ApJ, 661, 938
Brandt W.N. et al., 1994, ApJ, 424, 1
Broderick A. E., Finkbeiner D. P., Afshordi N., & Dobler G., 2007, *in prep.*
Calabretta M.R. & Roukema B.F., 2007, MNRAS, 381, 865
Davies R.D., Dickinson C., Banday A.J., Jaffe T.R., Górski K.M., & Davis R.J., 2006, MNRAS, 370, 1125
de Oliveira-Costa A., Kogut A., Devlin M.J., Netterfield C.B., Page L.A., & Wollack E.J., 1997, ApJ, 482, L17
de Oliveira-Costa A., Tegmark M., Page L., & Boughn S., 1998, ApJ, 509, L9
de Oliveira-Costa A. et al., 1999, ApJ, 527, L9
de Oliveira-Costa A. et al., 2002, ApJ, 567, 363
de Oliveira-Costa A. et al., 2004, ApJ, 606, L89
de Oliveira-Costa A. & Tegmark M., Phys. Rev. D, 2006, 74, 023005
Dennison B., Simonetti J.H., & Topasna G., 1998, Publ. Astron. Soc. Australia, 15, 147
Dobler G. & Finkbeiner D.P, 2007, in preparation
Dodelson S., ApJ, 1997, 482, 577
Drain B.T. & Lazarian A., 1998a, ApJ, 494, L19
Drain B.T. & Lazarian A., 1998b, ApJ, 508, 157
Drain B.T. & Lazarian A., 1999, ApJ, 512, 740
Eriksen H.K. et al., 2006, ApJ, 641, 665
Finkbeiner D.P., Schlegel D.J, Frank, C., & Heiles C., 2002, ApJ, 566, 898
Finkbeiner D.P., 2003, ApJS, 146, 407
Finkbeiner D.P., 2004, ApJ, 614, 186
Finkbeiner D. P., Langston G. I., & Minter A. H. 2004, ApJ, 617, 350
Finkbeiner D.P., Davis M., & Schlegel D.J., 1999, ApJ, 524, 867
Gaustad J.E., McCullough P.R., Rosing W., & Van Buren D., 2001, PASP, 113, 1326
Górski K.M., Hivon E., & Wandelt B.D., 1999, in MPA/ESO Cosmology Conf., Evolution of Large-Scale Structure, ed. A. J. Banday, R. K. Sheth, & L. N. da Costa (Garching: ESO), 37
Hansen F.K., Banday A.J., Eriksen H.K., Górski K.M., & Lilje P.B., 2006, ApJ, 648, 784
Haslam C.G.T., Stoffel H., Salter C.J., & Wilson W.E., 1982, A&AS, 47, 1
Haffner L.M., Reynolds R.J., Tufte S.L., Madsen G.J., Jaehnig K.P., & Percival J.W., 2003, ApJS, 149, 405
Hinshaw G. et al., 2007, ApJS, 170, 288
Hooper D., Finkbeiner D.P., & Dobler G., 2007, Phys. Rev. D, 76, 3012
Kogut A. et al., 1996, ApJ, 464, L5
Kogut A. et al., 2007, astro-ph/0704.3991
Page L. et al., 2007, ApJS, 170, 335
Press W. H., Teukolsky S. A., Vetterling W. T., & Flannery B. P., 1992, Numerical Recipes in C, 2nd edn. (Cambridge, UK: Cambridge University Press)
Schlegel D.J., Finkbeiner D.P., & Davis M., 1998, ApJ, 500, 525
Spergel D.N. et al., 2003, ApJS, 148, 175
Spergel D.N. et al., 2007, ApJS, 170, 377
Spitzer L. 1978, *Physical Processes in the Interstellar Medium*,
Tegmark M., de Oliveira-Costa A., & Hamilton A., 2003, Phys. Rev. D, 68, l3523
Tegmark M. et al., 2004, Phys. Rev. D, 69, 103501